Journal of Materials Chemistry A

PAPER

Cite this: J. Mater. Chem. A, 2018, 6, 5156

Investigation of the exceptional charge performance of the $0.93Li_{4-x}Mn_2O_5$–$0.07Li_2O$ composite cathode for Li-ion batteries†

M. Freire,[ae] M. Diaz-Lopez,[bc] P. Bordet,[bc] C. V. Colin,[bc] O. I. Lebedev,[a] N. V. Kosova,[d] C. Jordy,[e] D. Chateigner,[a] A. L. Chuvilin,[f] A. Maignan[a] and V. Pralong*[a]

Received 8th January 2018
Accepted 18th February 2018

DOI: 10.1039/c8ta00234g

rsc.li/materials-a

Herein, we report a detailed study on the high-energy density nanostructured $Li_{4-x}Mn_2O_5$–Li_2O composite with a high discharge capacity of 355 mA h g^{-1}, constituting the highest value reported to date for a lithium–manganese oxide electrode. Its high capacity was previously wrongly attributed to the participation of $Li_{4-x}Mn_2O_5$ (Li4) alone. However, more detailed compositional, structural, and electrochemical analyses revealed the important role played by Li_2O during battery cycling that was able to increase the original capacity of Li4 by 100 mA h g^{-1}. The participation of Li_2O is evident during the first charge when it is mixed on the nanoscale with lithiated manganese oxide. The fully delithiated phase Li0 is formed after the first charge. Our structural study combining neutron and synchrotron diffraction and transmission electron microscopy demonstrates that lithium exchange essentially implies breathing of the average cubic framework accompanied by small local atomic rearrangements that mainly involve oxygen anions.

Introduction

Electrochemical storage remains one of the major energy challenges, and to achieve higher energy and power densities, numerous studies have been targeted on the enhancement of the performance of rechargeable Li-ion batteries. In particular, research has been focused on new, non-toxic, low-cost, eco-friendly, and safer materials.[1–6] In the cathode, the extraction and insertion of lithium in the structure are accompanied by redox reactions, which are a function of the applied potential.

Despite extensive studies, only a few phases have been reported as attractive cathodes for Li-ion batteries within the Li–Mn–O system. The best-performing compounds are the spinel $LiMn_2O_4$,[7,8] exhibiting a 3D structure, and pure manganese 2D $LiMO_2$ layered materials. The layered compounds $LiMnO_2$ (ref. 9–11) and Li_2MnO_3 (ref. 12–14) have been extensively studied. They exhibit capacities of ~200 mA h g^{-1} and are characterized by an irreversible structural transformation upon cycling. The best electrochemical performance is displayed by layered materials containing a mixture of M transition metals, *e.g.* M = Mn, Ni, and Co: $Li_{1/3}Ni_{1/3}Mn_{1/3}CoO_2$ (NMC)[15] and $xLi_2MnO_3 \cdot (1-x)Li_{1/3}Ni_{1/3}Mn_{1/3}CoO_2$ composites[16–19] achieve reversible capacities higher than 250 mA h g^{-1}.

In the case of Li-rich composites such as $(1-x)Li_2MnO_3 \cdot xLiMO_2$, where M = Ni, Mn, and Co, or $Li_{1+x}Ni_yCo_zMn_{1-x-y-z}O_2$ compounds,[20–22] the overlithiated Li_2MnO_3 component not only acts as a structural stabilizing agent, but also, most importantly, can provide anomalous capacities (over 250 mA h g^{-1}) after electrochemical activation above *ca.* 4.5 V.

The electrochemical performance of the aforementioned materials in terms of capacity is limited to one electron per transition metal (TM) atom. However, several Li-rich materials exhibit delithiation extent beyond the conventional limit given by the TM redox reactions; this leads to additional capacity. In these compounds, reversible redox processes and high irreversible capacities (irreversible oxygen losses) are observed. To explain the high capacities[23–25] often observed in overlithiated materials, the electrochemical activity of cumulative cationic $M^{n+} \rightarrow M^{(n+1)+}$ and anionic $2(O^{2-}) \rightarrow (O_2)^{n-}$ reactions is needed. The simultaneous extraction of lithium and oxygen from the structure occurs together with the activation of the material induced by charging above 4.5 V (often associated with a voltage plateau). In fact, the oxidation of oxygen and the formation of peroxo/superoxo groups are related to the possible release of oxygen molecules. Lu and Dahn[26] have explained charge compensation in $Li/Li[Ni_xLi_{(1/3-2x/3)}Mn_{(2/3-x/3)}]O_2$ on the basis of the loss of oxygen and leaching of

[a]Laboratoire de Cristallographie et Sciences des Matériaux CRISMAT, ENSICAEN, Normandie Université, CNRS, Université de Caen Normandie, 6 Bd Maréchal Juin, F-14050 Caen, France. E-mail: valerie.pralong@ensicaen.fr
[b]Université; Grenoble Alpes, Institut Néel, F-38000 Grenoble, France
[c]CNRS, Institut Néel, F-38000 Grenoble, France
[d]Institute of Solid State Chemistry and Mechanochemistry SB RAS, 18 Kutateladze, Novosibirsk 630128, Russia
[e]Saft, Direction de la Recherche, 111/113 Bd Alfred Daney, 33074 Bordeaux, France
[f]CIC nanoGUNE, 20018 Donostia-San Sebastian, Spain

† Electronic supplementary information (ESI) available: X-ray diffraction data for electrochemically charged and chemically oxidized $Li_{4-x}Mn_2O_5$. PDF simulation of a main $Li_4Mn_2O_5$ phase. See DOI: 10.1039/c8ta00234g

Li_2O during the first oxidation. Interestingly, Okamoto[27] confirmed from first-principles calculations that the presence of oxygen vacancies in Li_2MnO_3 would decrease the redox potential associated with lithium extraction. Similarly, Bruce *et al.*[28] have demonstrated that lithium extraction in $Li_{1.2}[Ni_{0.13}Co_{0.13}Mn_{0.54}]O_2$ is charge-compensated by electron holes localized on the oxygen atoms coordinated by Mn^{4+} and Li^+. The loss of oxygen on the surface[16,17] is accompanied by the diffusion of TM ions away from the surface into the bulk to enter octahedral sites in the TM layers. It is worth noting that within a crystal, different local environments have an impact on the redox processes and consequently on the participation of oxygen. *Via* DFT calculations, Ceder *et al.*[29] have shown that a local excess of lithium in the environment of oxygen anions increases the labile character of oxygen electrons, which can be more easily extracted and thus become able to participate in redox reactions. Moreover, the nucleation of a distorted and/or disordered phase results in the modification of the oxygen network. On the other hand, the oxidation of oxide ions in these layered manganese-based materials results in a partial loss of oxygen with irreversible structural modifications (*e.g.* the formation of Li_2O as a byproduct), and the solid-state redox reactions of the oxide ions are stabilized in ruthenium-based $Li_2Ru_{1-y}Sn_yO_3$, with the oxidation of O^{2-} to the peroxo-like species $(O_2)^{n-}$. This feature was experimentally proved without any ambiguity by Tarascon *et al.*[30–33] These results were further supported by Islam *et al.*,[34] who showed that the formation of O–O bonds and $(O_2)^{n-}$ species in highly delithiated states in Li_2MnO_3 was due to d–p hybridization. The presence of an electron hole on oxygen is an evidence for the oxidation of oxygen anions induced by the holes along the Li–O–Li configurations induced by an excess of lithium and cation disorder, *i.e.* with the extraction of a labile electron from oxygen anions; in addition, nanostructured active powders as well as intercalation compounds are widely used to improve the electrochemical performance of electrodes (for reviews see ref. 35 and 36).

Recently, we have reported a novel Li4 material with a disordered rock salt-type structure.[37] The meticulous compositional and sample purity analyses presented in this study allowed us to identify the composition of Li4 to be $0.93Li_{3.6}Mn_{2.4}O_{5.4}$–$0.07Li_2O$ (herein referred as a Li4–Li_2O composite).

The electrochemical performance of Li4 with and without Li_2O was evaluated, revealing that the presence of Li_2O in the composite was required to achieve the previously reported high discharge capacity of 355 mA h g^{-1}[37]. To gain a better understanding of the mechanism at work in the lithium extraction process involved in the Li4–Li_2O composite, we conducted a thorough structural investigation using experimental techniques adapted according to its nanostructured nature and coupled with electrochemical characterizations. The results of these investigations for pristine and oxidized samples are presented in this study.

Experimental

Nanostructured Li4–Li_2O composite and $Li_{3.6}Mn_{2.4}O_{5.4}$ (Li4) were synthesized by a two-step route using mechanochemical activation. At first, high-temperature $LiMnO_2$ (HT-$LiMnO_2$) was produced by a solid-state reaction using a reagent mixture of LiOH, MnO_2, and MnO, with the molar ratio of 2 : 1 : 1, which was ground energetically. A small excess (~5 wt%) of LiOH was added to compensate for the evaporation of lithium at high temperatures. Then, the homogeneous mixture was heat-treated at 1000 °C under an argon flow for 8 h. The mechanochemical synthesis was carried out using Fritsch Planetary Micro Mill PULVERISETTE 7 premium at 700 rpm inside a 20 mL tungsten carbide bowl with four WC grinding balls (with a diameter of 10 mm). Then, $LiMnO_2$ (4.32 g) was ground with a stoichiometric amount of Li_2O (0.68 g) for 20 h, and 5 wt% of carbon black was added after 15 h of mechanical milling to improve the electrochemical performance and electronic conductivity upon cycling.

To produce a large amount (2.5 g) of the oxidized phase required for neutron powder diffraction experiments, the as-prepared material was chemically oxidized with an excess of NO_2BF_4 (5.2 V *vs.* Li^+/Li) in acetonitrile for 7 days under stirring. The product of the reaction was washed with acetonitrile. This synthetic route produced samples that were identical to the electrochemically charged Li0 (see Fig. SI-1†).

The electrochemical performance was tested with Swagelok cells using lithium as a counter electrode. For electrochemical measurements, composite electrodes were made by grinding the Li4–Li_2O nanopowder with carbon black (weight ratio of 72 : 28). The electrolyte, namely, $LiPF_6$ (1 M), was dissolved in EC (ethylene carbonate) + EMC (ethyl methyl carbonate) with a volume ratio of 3 : 7. The cells were assembled in an argon-filled dry glove box with a typical loading of 20–25 g cm^{-2} of the active material. The electrochemical studies were carried out at room temperature (RT) using a VMP II potentiostat/galvanostat (Biologic SA, Claix, France) at a slow cycling rate of the extraction/insertion of 1 Li^+ ion in 20 hours (corresponding to a rate of C/80 if we consider the extraction/insertion of 4 lithium ions) in the galvanostatic mode between 1.2 V and 4.8 V. Unless otherwise stated, the cycling rates used in this study correspond to the removal/insertion of 1 Li^+ in 20 hours. This slow rate, close to the thermodynamic conditions, has been found to facilitate the understanding of the electrochemical processes involved during the charge–discharge cycles.

The long-term cycling capability of the composite electrode was studied in coin cells using a mixture of 70 wt% of the active material (Li4–Li_2O), 10 wt% of carbon black, and 20 wt% of polytetrafluoroethylene (PTFE) binder and applying the previously specified cut-off voltages.

Neutron powder diffraction (NPD) patterns were acquired at the French CRG-D1B beamline at the Institut Laue-Langevin with the monochromatized wavelength of 1.288 Å (see Fig. SI-2†). Approximately 1.5 g of powder was prepared in a cylindrical vanadium can with a diameter of 5 mm sealed under an inert Ar atmosphere. The data were obtained at room temperature in the 2θ range of 1.0–125.0° with a data collection time of 2 h per sample. Calibration of the instrument resolution function was carried out with a $Na_2Ca_3Al_2F_{14}$ (NAC) standard.

High-energy synchrotron X-ray powder diffraction (HE-SXRPD) patterns with a high spatial resolution were acquired

at the French CRG-D2AM beamline (BM02) using $\lambda = 0.4959$ Å radiation for subsequent Rietveld and PDF analysis. The samples were prepared under inert conditions in epoxy-sealed borosilicate glass capillaries with an outer diameter of 0.7 mm. The data were obtained at room temperature in the 2θ range of 0.8–128.0° with a data collection time of 2 h using the 2D pixel detector XPAD3.[38] To obtain data over this wide range of angles, 120 diffraction images were taken at each 2θ degree interval. These were assembled, averaged, and rebinned using the PyFAI[39] software to produce a single 1D pattern. In addition, the diffraction pattern of an empty capillary was obtained. The data were calibrated by collecting data for a LaB_6 standard for 4 h. A Ni standard sample was also used to calibrate the experimental effects on the PDF data.

Rietveld refinements of the NPD and SXRPD data were performed with the FullProf software.[40] In addition, the SXRPD data were corrected and Fourier-transformed using the PDFgetX3 software[41] with $Q_{max} = 21.4$ Å^{-1}. Refinements of the PDF data were carried out with the PDFgui[42] software.

Transmission electron microscopy (TEM), including high-angle annular dark-field scanning TEM (HAADF-STEM) and annular bright-field STEM (ABF-STEM) studies, was carried out using the JEM-ARM200F cold FEG microscope corrected for spherical aberration and probe corrected microscope, equipped with a large-solid-angle CENTURIO EDX detector and a Quantum EELS spectrometer. Crushed samples in a suspension with butanol were deposited on porous carbon grids in an argon-filled glove box. Due to the high sensitivity of these materials to high temperatures and to avoid destruction of the sample by the electron beam during TEM measurements, 80 kV voltage conditions were used.

Elemental analyses of the as-prepared and oxidized materials were carried out using an inductively coupled plasma optical emission spectrometer (ICP-OES; Agilent 5100). The active material was completely dissolved in a concentrated aqua regia solution for several hours until it became clear. This solution was further dissolved in a ratio of 1 : 5 and filtered with nylon filters with a pore diameter of 0.45 μm.

Results and discussion

Electrochemical investigation

The as-prepared nanostructured Li4–Li_2O composite displayed remarkable electrochemical performance. Fig. 1 shows the charge–discharge profiles, in which the oxidation process during charging is achieved by a gradual increase in the cut-off voltage from 4.4 V to 4.6 V and later to 4.8 V. The electrochemical activity of the Li4–Li_2O composite displayed substantial irreversibility in the first cycle: the capacity of ~348 mA h g^{-1} in the first charge to 4.4 V corresponds to the extraction of 2.83 Li^+/f.u, and the average capacity of 287 mA h g^{-1} in the first discharge to 1.2 V corresponds to the reinsertion of 2.33 Li^+/f.u. Thus, an irreversible capacity of 61 mA h g^{-1} corresponding to ~0.5 Li^+ was observed, which indicated an open-circuit voltage (OCV) of 1.9 V. Improvements in reversibility and capacity retention were observed after the first cycle. After three cycles, the capacity reached a high value of 303 mA h g^{-1}, corresponding to the reinsertion of 2.47 Li^+/f.u. upon discharge.

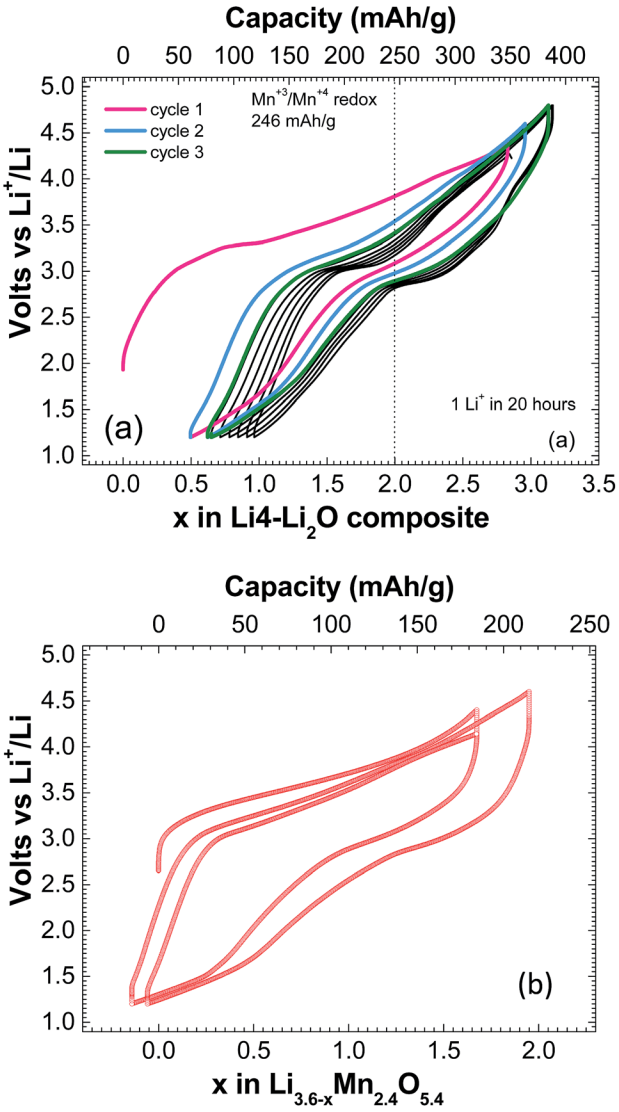

Fig. 1 Typical voltage–composition profile of the Li4–Li_2O composite (a) and Li4 (b).

The composition of the active Li4 material was identified to be $Li_{3.6}Mn_{2.4}O_{5.4}$.‡ The synthesis of Li4 was achieved without any trace of a Li_2O impurity (Fig. SI-1†), and the electrochemical curve of the Li4 material was studied (Fig. 1b). The reversibility of the Li4 material was significantly enhanced in the absence of Li_2O, although the discharge capacity decreased by ~30%. These results indicate the participation of the Li_2O phase in the electrochemical performance of Li4–Li_2O.

‡ Chemical analyses. The Li : Mn ratios in the as-prepared and oxidized materials were determined using ICP elemental analyses. The proportion of Li : Mn was equal to 1.9 ± 0.05 for the Li4–Li_2O composite and 0.2 ± 0.05 for the oxidized Li0 material. These results confirm that the delithiation process occurred during the charge of the as-prepared material and thus provided other constraints for the Rietveld refinement.

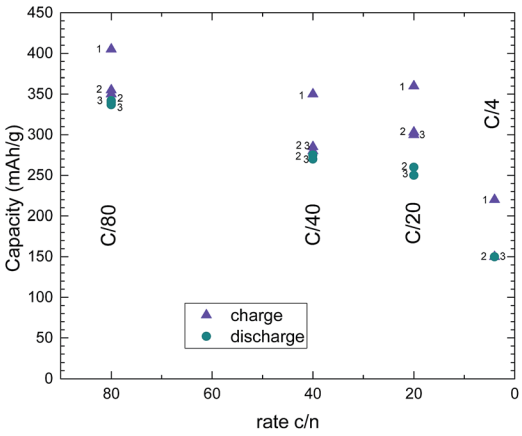

Fig. 2 Capacity *vs.* capacity rate for the Li4–Li_2O composite for the first three cycles.

Fig. 2 shows the discharge capacity of Li4–Li_2O for the first three cycles at several current rates ranging from C/80 to C/4. The discharge capacity was highest at the slowest studied rate, namely, C/80. The stable discharge capacities at C/40 (1 Li^+ in 10 hours) and C/20 (1 Li^+ in 5 hours) were relatively similar at ~270 mA h g^{-1}. The discharge capacity drastically decreased to 150 mA h g^{-1} at C/4 (1 Li^+ in 4 hours), with a significant increase in polarization. Note that in this preliminary study of the Li4–Li_2O composite, the performance was measured without optimization of the electrodes (*i.e.* in the absence of any slurry or binder). Thus, these results indicate a relatively satisfactory cycling stability of the composite at higher cycling rates up to 1 Li^+ in 5 hours.

The enhanced performance of the composite electrode at slower cycling rates could also be attributed to the longer time needed for the reaction of Li_2O, which was proven to play a key role in the achievement of high capacities (Fig. 1).

The disappearance of the Li_2O diffraction peaks in the case of Li0 might alternatively be attributed to the decomposition of Li_2O accompanied by the release of O_2. However, this scenario cannot explain the additional capacity retained beyond the first charge cycle as the capacity of the composite after the third cycle (see Fig. 1a) is ~100 mA h g^{-1} higher than that of Li4 without Li_2O (Fig. 1b). In addition, nanostructured Li_2O prepared in the same way as Li4 did not exhibit any electrochemical activity in the same potential window; this suggested that the presence of manganese oxide was needed to make Li4 active. The mechanism by which Li_2O is able to enhance the performance of the composite is not yet understood and requires further clarification.

Operando diffraction experiments and compositional and structural analysis of the sample obtained after the first charge–discharge cycle with reversible capacity were being performed at the time of writing this report, which would help to clarify the interaction between Li4 and Li_2O during the first charge.

The longer-term cycling of the Li4–Li_2O composite was studied up to 45 cycles (see Fig. SI-3†), and a stable discharge capacity of 190 mA h g^{-1} was observed (corresponding to the insertion of 1.65 Li^+), which constituted approximately 50% of the initial charge capacity. In addition, an increase in polarization was observed between the fifth cycle (350 mV) and the forty-fifth cycle (500 mV). Note again that these electrochemical tests were performed without optimization of the electrode.

Several electrochemical processes are observed in the cyclic voltammetry curves shown in Fig. 3. The first oxidation profile differs from the others and appears to be irreversible. This behavior may be ascribed to the reaction of Li_2O during the first electrochemical oxidation to 4.4 V.

During the second charge, a broad peak centered at 3.29 V *vs.* Li^+/Li appeared, which shifted to lower potentials in the subsequent cycles. This is a characteristic feature of the Mn^{3+}/Mn^{4+} redox couple. The peak centered at 4.0 V could be ascribed to Mn^{4+}/Mn^{5+} (unlikely, owing to the instability of Mn^{5+} in an octahedral environment) and/or O^{2-}/O^- couples (Fig. 3).

The electrochemical behavior of Li4–Li_2O was further characterized *via* cycling with a focus on the Mn^{3+}/Mn^{4+} redox couple, *i.e.* with extraction limited to two Li^+ ions, corresponding to the potential window of 1.5–3.7 V. Under these conditions, the oxidized phase with Mn^{4+} is obtained at ~3.7 V *vs.* Li^+/Li. The participation of oxygen, usually occurring at 4.5 V in Li-rich layered materials, was not observed, and we then focused on the redox activity of the Mn^{3+}/Mn^{4+} couple. The electrochemical process between Mn^{3+} and Mn^{4+} led to a low irreversible capacity of approximately 20 mA h g^{-1} (0.18 Li^+/f.u.) after the first cycle, and a discharge capacity of 230 mA h g^{-1} (Fig. 4a). However, the obtained polarization (>300 mV) was not reduced in comparison with that observed for the Li4–Li_2O composite (~300 mV) cycled between 1.2 V and 4.8 V, which involved the electrochemical activity of oxygen.

Thus, we needed to identify other redox-active centers involved in the course of the first charge involving almost three electrons (>350 mA h g^{-1}), which enabled the achievement of a reversible stable capacity of 275 mA h g^{-1} after 8 cycles (Fig. 1).

Galvanostatic intermittent titration technique (GITT) measurements provide information on the polarization evolution and relaxation kinetics, which enable the estimation of the internal resistance of the cathode during cycling, after each

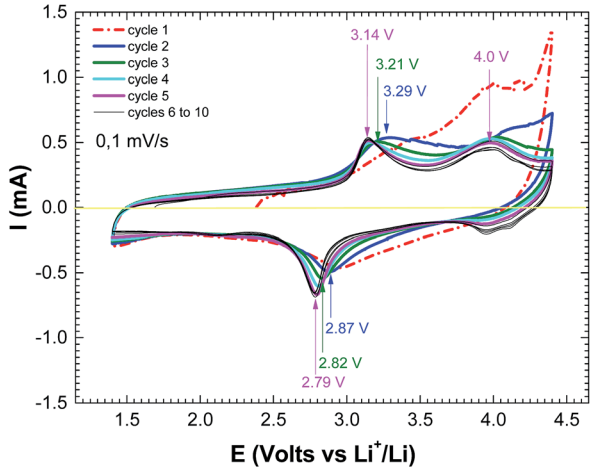

Fig. 3 Cyclic voltammetry curves for the first ten cycles for Li4–Li_2O at a rate of 10 mV s^{-1}.

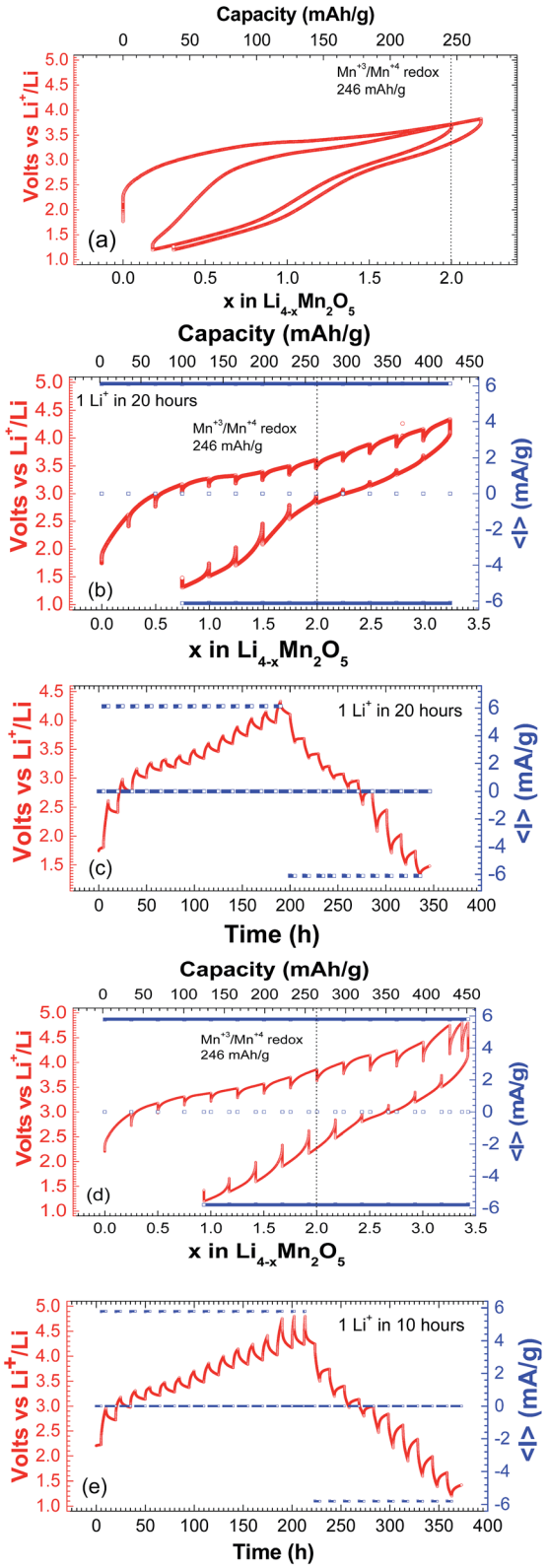

Fig. 4 (a) Typical voltage–composition profile of Li4–Li_2O obtained at C/80 involving only the Mn^{3+}/Mn^{4+} redox couple; GITT curves for the first cycle (between 1.2 and 4.4 V) as a function of (b) the composition and (c) the time at a rate equal to C/80, with a charging (discharging) time of 5 h followed by a relaxation time of 10 h; and GITT curves for the first cycle (between 1.2 and 4.8 V) as a function of (d) the composition and (e) the time at a rate equal to C/40, with a charging (discharging) time of 5 h followed by a relaxation time of 10 h.

current step, and before the relaxation period. During the first cycle (Fig. 4b–e), the variation in the potential ΔU during the relaxation period was approximately constant in the charge process (~200 mV), whereas in the following discharge process, ΔU increased from 80 mV to 400 mV at the end of the reduction process. The evolution of this potential after each step suggests a contribution from an additional phenomenon other than charge transfer. These results indicate the coexistence of various processes with different kinetics during the first cycle.

When the composite electrode was charged directly up to 4.8 V (Fig. 4d–e), an increase in polarization at potentials higher than 4.2 V was observed in comparison with that in the potential window between 1.5 V and 3.7 V. During the subsequent discharge to 1.2 V, this parameter decreased and reached a minimum value of ~2.5 V. At potentials higher than 4.5 V, we noticed an increase in polarization after each current step presumably due to a kinetically different process such as the degradation of the electrolyte. GITT measurements are used to monitor the phase transformation of the electrodes and enable the determination of the lithium ion diffusion coefficient during cycling that is strongly influenced by the particle size (see ref. 43 and 44). At the rates of C/80 and C/40, the diffusion coefficient D_{Li^+} of nanostructured Li4–Li_2O lies within the range of 10^{-10} to 10^{-9} cm^2 s^{-1}, comparable to the D_{Li^+} values for LNMC and $LiFePO_4$.[45] This high diffusion coefficient of the composite could be related to nanostructuring and intrinsic disorder in Li4.

Structural investigations

To better understand the oxidation processes occurring in the course of the first charge, the as-prepared and chemically oxidized materials were studied in depth using complementary structural investigation techniques: combined Rietveld refinements of SXRPD and NPD data, PDF analysis of SXRPD data, and HAADF-STEM observations.

The atomic coordinates of a rock-salt MnO-type structure with modified occupancy values were used as a starting model for combined NPD and SXRPD Rietveld refinements for the as-prepared and chemically oxidized samples. The same structural model and microstructural parameters were used to simultaneously refine both sets of data.

The scale factor, lattice parameters, and independent isotropic thermal parameters B_{iso} for cation and anion sites were refined. The backgrounds were fitted with Chebyshev polynomials. The profile shapes were described using a modified Thompson–Cox–Hastings pseudo-Voigt function,[46] where instrumental profiles were determined by the refinement of standards. Line-broadening anisotropy was attributed to anisotropic coherent size domains. To describe this effect, we used a spherical harmonic expansion (SPH) of the Scherrer formula with the Laue class symmetry of *m*3*m* as implemented in FullProf. The domain microstrains were refined isotropically. Peaks due to the Li_2O component were observed in the NPD and SXRPD patterns of Li4, for which the refined weight percentage amounted to 7.2(3)%. For Li0, the regions between 10° and 12° and between 16° and 18° in the SXRPD pattern were excluded

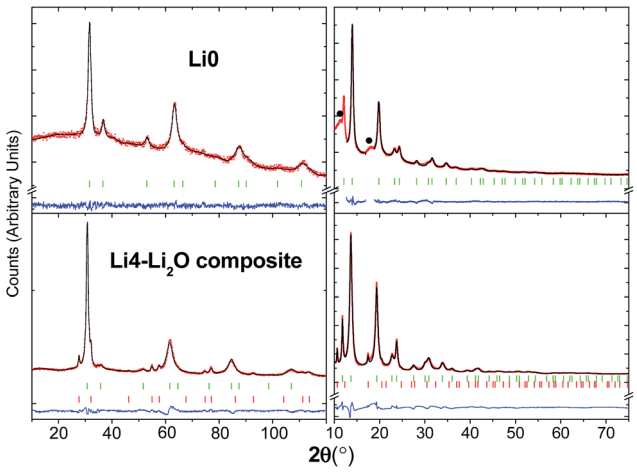

Fig. 5 Combined Rietveld refinements of (left) NPD and (right) SXRPD data for (top) Li0 and (bottom) the Li4–Li_2O composite. For the X-ray data, the diffraction peaks due to an unknown phase are represented by the symbol ●. The green and orange tick marks correspond to $Li_{4-x}Mn_2O_5$ and Li_2O, respectively.

from the refinement owing to the presence of two broad peaks, which could not be assigned to a known phase and could not be observed in the NPD data. An excellent fit to the experimental profile was obtained (Fig. 5) for both the starting sample and the delithiated sample. The refined crystallographic data and reliability factors are presented in Table 1.

For the refinement of the as-prepared sample, the Mn cation valence was fixed at 3+, the atomic occupancies were then allowed to vary as $Li_{4-x}{}^{+}Mn_{2\mp x}{}^{3+}O_{5\mp x}{}^{2-}$, and the overall Li : Mn ratio (taking into account the loss of lithium in the main phase by the formation of an Li_2O impurity) was constrained to be 2 : 1 as determined by ICP, yielding $Li_{3.59(2)}Mn_{2.41(2)}O_{5.41(2)}$. For the chemically oxidized sample, in the first instance, the manganese and oxygen contents were considered to be unchanged, and the lithium content was refined as $Li_{3.6-x}Mn_{2.4}O_{5.4}$. The refined value of $x = 3.6(1)$ is in good agreement with that derived from the voltage–composition profile shown in Fig. 1a and the ICP results. We then investigated the possibility of oxygen loss by fixing the Li and Mn occupancies at their previous values (*i.e.* 0 and 2.4, respectively) and allowing the stoichiometry of the sample to vary as $Mn_{2.4}O_{5.4-y}$. The final refined composition of $Mn_{2.4}O_{5.0(1)}$ could indicate the possible release of oxygen during oxidation. Although the occurrence of the release of a sizeable amount of oxygen is an important issue for the elucidation of the oxidation mechanism, the present result should be taken with great care. In fact, the refinement of the oxygen occupancy did not improve the fits significantly, *i.e.* the R_{wp} values decreased by only ~3% and the R_{Bragg} values increased by more than 8% when the oxygen content was refined. Moreover, owing to the small number of observable Bragg reflections and the disordered nature of the material, the precision achieved by the Rietveld refinement of occupancy parameters was intrinsically limited and inevitably smaller than that deduced from the calculated e.s.d. values.

Table 1 Details from the combined Rietveld refinements of Li4–Li_2O and Li0. The values in parentheses are 1 e.s.d. for the last digit

		Li4	Li0
		$Li_{4-x}{}^{+}Mn_{2+x}{}^{3+}O_{5+x}{}^{2-}$	$Mn_{2.4}O_{5.4-y}$
x		$x = 0.41(2)$	—
y		—	$y = 0.4(1)$
Rietveld refined parameters and agreement factors			
a (Å)		4.1678(2)	4.0681(1)
$B_{iso,O}$ (Å^2)		1.94(2)	2.07(6)
$B_{iso,Mn}$ (Å^2)		0.35(1)	0.55(4)
Coherent domain size (nm)		7.34(8)	6.93(2)
NPD	R_{wp} (%)	10.7	24.9
	R_{Bragg}	1.70	6.69
SXRPD	R_{wp} (%)	11.2	8.12

The Rietveld refined structures were used as starting points for modelling the PDF data of the two samples investigated herein. The short (1–10 Å) and long (10–35 Å) r-ranges were fitted separately with PDFgui. The PDFs displayed no peaks ascribed to the presence of impurities, and due to the low fraction of the Li_2O phase found by Rietveld refinement, only the main Li4 phase was considered (Fig. SI-5†). The instrumental dampening and broadening of the PDF signal were quantified by modeling a nickel standard. The scale factor, linear correlation factor $\delta 1$, lattice parameters, particle size, and overall isotropic atomic displacement factor for all atoms $B_{iso,ov}$ were refined for the long r-range, and the data rendered a good agreement with the average rock salt-type model (Fig. 6). The reasonable refined parameters and acceptable R_w values obtained herein (Table 2) confirm once again that despite the presence of a large amount of disorder in $Li_{3.6-x}Mn_{2.4}O_{5.4}$, its average structure remains analogous to that of MnO.

A comparison of the experimental PDF data for the range between 1 and 10 Å with those calculated from the previously

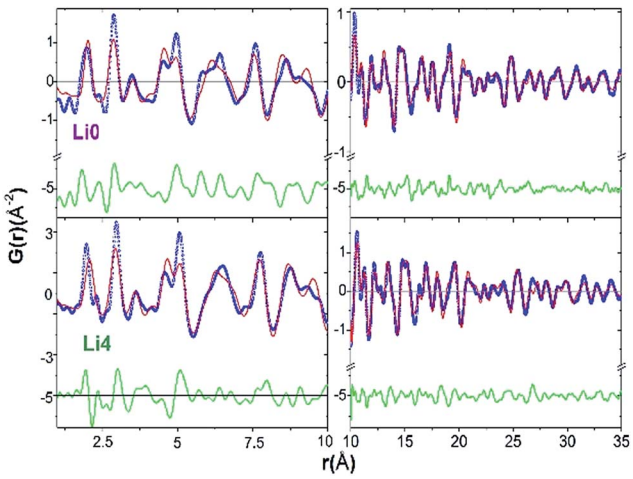

Fig. 6 (Right) PDF refinements for (top) Li0 and (bottom) Li4 between 10 and 35 Å using an average cubic MnO model; (left) comparison for the r-range below 10 Å of the PDF data observed and calculated using the same model, showing local distortions.

Table 2 Details from the x-PDF fits for $Li_{3.6-x}Mn_{2.4}O_{5.4}$

Space group	$Fm\bar{3}m$			
Sample ID	Li4		Li0	
Composition	$Li_{3.6}Mn_{2.4}O_{5.4}$		$Li_0Mn_{2.4}O_5$	
Fitted *r*-range (Å)	1–10	10–35	1–10	10–35
R_w	0.448	0.322	0.450	0.293
Coherent domain size (nm)	4.8 (fixed)	4.8(9)	5.2 (fixed)	5.2(8)
a (Å)	4.160 (fixed)	4.160(3)	4.065 (fixed)	4.065(4)
$\delta 1$	1.0(2)	1.0 (fixed)	1.4(2)	1.4 (fixed)
$B_{iso,ov}$ (Å^2)	1.4(2)	1.4(2)	1.6(3)	2.5(3)

refined average models for the range of 10–35 Å led to unsatisfactory agreement factors and poor fits, which were symptomatic of local structural disorder (Fig. 6), left. For both samples, calculations based on refinements for the long *r*-range were not able to reproduce the PDF data observed for the short *r*-range (see, for instance, the peak at 2 Å). To qualitatively visualize the effects of the local disorder, the *r*-scale for Li0 was multiplied by the lattice parameter ratio (a_{Li4}/a_{Li0}) determined from the long-range PDF fits. The results are shown up to 10 Å at the bottom of Fig. 7. This rescaling is meaningful because the structure has a cubic symmetry, and all interatomic distances are proportional to the cell parameter. Upon the removal of Li, breathing of the average structure was observed. A decrease in the cell parameter from 4.170 to 4.069 Å for Li4 and Li0, respectively, was induced by the increase in the valence of Mn and the presence of almost 2/3 vacancies at the cation sites. This breathing process was accompanied by clear modifications of the local structure that mainly involved oxygen anions, whereas the cation network seemed to preserve its cubic arrangement. As seen in Fig. 7, the peaks corresponding to Mn–Mn distances were barely modified, whereas those for Mn–O distances were displaced and distorted. The latter point was confirmed by the HAADF-STEM analysis mentioned in the following section. The structural coherence length of about 6 nm, in good agreement with the Rietveld refinements, was not markedly modified by the removal of Li (Fig. SI-6†). Thus, our results indicate that Li exchange can proceed without major structural rearrangements as required for the good cyclability of cathode materials.

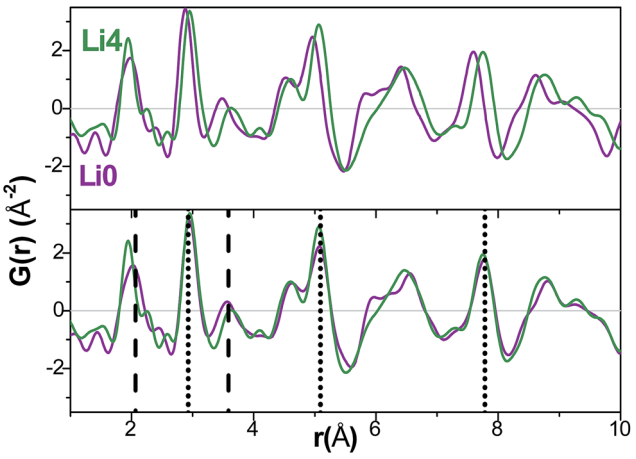

Fig. 7 (Top) Comparison of the PDF data for Li4 (green) and Li0 (purple) for the short *r*-range. In the bottom panel, the distances for Li0 have been rescaled by the ratio of the cell parameters of the two compounds (see main text). The Mn–O and Mn–Mn distances from the average rock salt model are shown as dashed and dotted lines, respectively.

However, the oxygen coordination polyhedra of the cations have to adapt to the change in valence that accompanies the removal of Li. A higher degree of disorder among oxygen sites is further supported by the higher thermal parameters determined by Rietveld refinement (Table 2) for the two compositions studied herein. Already for Li4, the cation coordination was modified with respect to a regular octahedron, as evidenced by the splitting of the first PDF peak centered at 2 Å (Fig. SI-7†). According to the refined cell parameter of the average cubic structure, this peak should be at 2.08 Å; however, it appears to split into one strong peak at 1.97 Å and a smaller peak at 2.31 Å. Since the ionic radii of Mn^{3+} in 5- and 6-fold coordination (0.58 Å and 0.645 Å (ref. 47)) correspond to the Mn–O distances of 1.98 and 2.07 Å, respectively, the strong peak may be attributed to Mn–O bonds. The smaller peak at 2.31 Å could be ascribed to the Li–O bonds although these appear to be a little longer than expected from the ionic radius of Li^+. This attribution is supported by the disappearance of this peak in the pattern of the delithiated sample. The fitting of the intensity ratio of the two peaks with a Gaussian function yields a ratio of 4.29, whereas the ratio calculated from the stoichiometry of Li4 and the number of electrons on the Mn and Li atoms is 4.16, assuming equivalent coordination for both species. This does not preclude the possibility of a contribution to the peak at 2.31 Å from local distortions of the MnO_6 octahedra induced by structural disorder and/or Jahn–Teller distortion of Mn^{3+} cations.

For the chemically oxidized compound, the first peaks at 2.0 and 1.8 Å can be fitted with two Gaussian functions with an intensity ratio of 9 : 1. The former is compatible with Mn^{4+} cations in octahedral coordination (bond distance from ionic radius: 1.93 Å), whereas the latter is compatible with Mn^{4+} or Mn^{5+} cations in tetrahedral coordination (bond distances: 1.79 or 1.73 Å, respectively). Indeed, only octahedral or tetrahedral coordination is reported for Mn^{4+} cations, and only tetrahedral coordination is reported for Mn^{5+} cations. However, this attribution has to be regarded with great care because the intensity ratio of these two peaks is not consistent with a Mn valence

close to 4.5. In fact, the weakness of the peak at 1.8 Å makes the presence of tetrahedrally coordinated Mn^{4+} or Mn^{5+} cations unlikely. This would also require a drastic structural rearrangement of the oxygen framework, which is observed neither in the PDF nor in the TEM experiments. On the other hand, the possible presence of peroxo anions (O_2^{n-}) in the structure would strongly distort the coordination polyhedra of Mn, leading to deformation of the first neighbour peak in the PDF pattern. However, this study was limited by the low sensitivity of X-rays for Li and O atoms. A full characterization of the local structure combining the current data with NPD PDF data is ongoing and will be reported in the future.

To investigate structural features at the atomic level, HAADF-STEM and ABF-STEM were performed on the as-prepared Li4–Li_2O and oxidized Li0 materials (Fig. 8 and 9).

The simultaneous examination of HAADF-STEM and ABF-STEM images allows the simultaneous visualization of heavy (Mn) and light (Li, O) atoms, respectively. The refined structural model detailed in Table 2 was used for the simulations.

High-resolution HAADF-STEM (Fig. 8a) and ABF-STEM (Fig. 8b) images demonstrate the high crystallinity of the as-prepared Li4 domains, which are well ordered at the atomic level with punctual atomic columns. The slight variation in the brightness of the Mn/Li columns in the HAADF-STEM image (Fig. 8a) can be attributed to an inhomogeneous distribution of Li and Mn atoms. It is important to note that a quite homogeneous contrast is observed in the ABF-STEM image, where the black dots correspond to the Li/Mn columns and the grey dots correspond to the O columns according to image simulations. This indicates that all atoms are located close to their expected positions in the rock salt structure, and local atomic displacements are small, which is in good agreement with the results obtained from the NPD and SXRPD experiments.

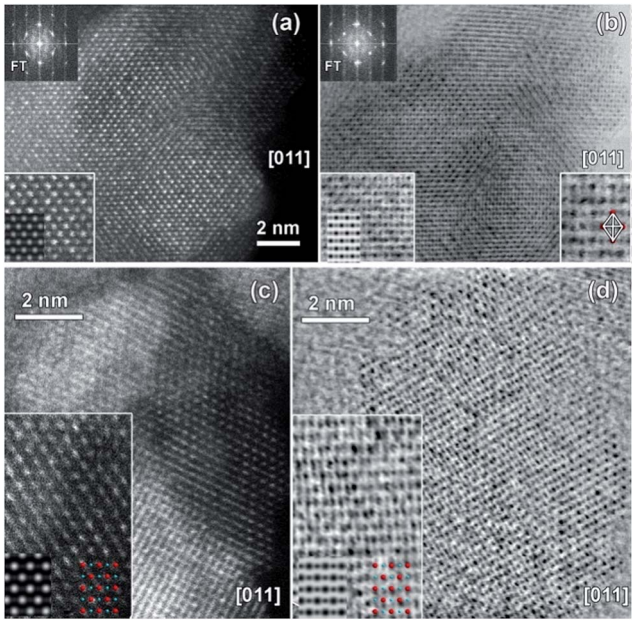

Fig. 8 (a) [011] HAADF-STEM and (b) ABF-STEM images of the as-prepared Li4–Li_2O with the corresponding FT patterns shown in the top left corner. The bottom left insets show magnifications with a Li/Mn (90/10) simulation overlay on top. The bottom right inset in (b) corresponds to a magnified ABF-STEM image in which a Li/Mn octahedron has been drawn. (c) and (d) [011] HAADF-STEM and ABF-STEM images of the chemically oxidized Li0, respectively. The bottom left insets show magnifications with a Li/Mn (5/95) (see model S1†) simulation overlay on top. Li/Mn atoms are represented by red spheres and O atoms are represented by blue spheres.

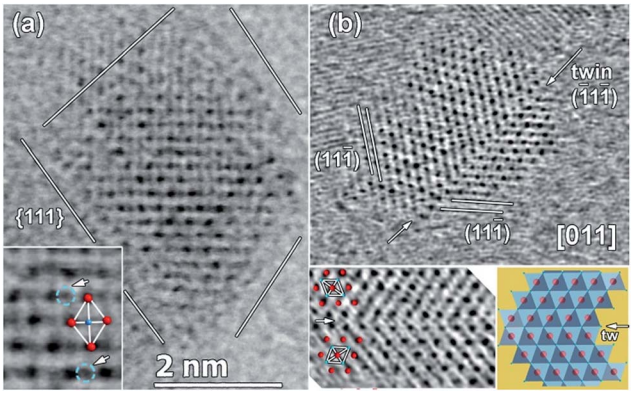

Fig. 9 [011] ABF-STEM images of the chemically oxidized Li0. (a) Single nanoparticle: the inset shows a magnified image showing the structural model (Li/Mn: red, O: blue). The white arrows indicate the displacement of the oxygen atoms circled in blue dashed lines towards Mn atoms; (b) twinned nanoparticles: the bottom left inset shows a magnified image of the structural model, and the bottom right inset shows an isolated (111) twin plane (white arrow).

HAADF-STEM (Fig. 8c) and ABF-STEM (Fig. 8d) images of the chemically oxidized Li0 also display a rock salt-type structure. However, a more homogeneous contrast is observed in the HAADF-STEM image (Fig. 8c) with respect to that of Li4 (Fig. 8a). The increased homogeneity in the HAADF-STEM image shown in Fig. 8c is ascribed to the almost exclusive presence of Mn atoms along the columns due to the removal of Li. On the other hand, the increased disorder in the ABF-STEM images shown in Fig. 8d can be explained by a more pronounced disorder of the oxygen atoms that form the coordination polyhedra around Mn cations with various valences and coordination numbers and is also possibly related to the presence of peroxo anions. This is consistent with the conclusions from the diffraction/PDF study reported above.

TEM images are projections of the structure onto a plane. The determination of the displacements of single atoms from the atomic column that represents their average position is difficult in a thick sample. Therefore, we performed ABF-STEM imaging on a single Li0 nanoparticle.

Fig. 9a shows an ABF-STEM image of a single Li0 nanoparticle with a size of 2.5–3 nm. The particle has an octahedron-like shape faceting along the {111} planes. The evident inhomogeneity is due to a high degree of local disorder and the displacement of oxygen atoms. The inset in Fig. 9a shows a clear shift of an oxygen atom from its ideal octahedral position towards the Mn column. Note that all other O atoms in the same octahedron remain at their ideal positions; this suggested a lack of octahedral tilting. The displacement of certain oxygen atoms away from their ideal positions towards the Mn column could be induced by strong TM–O hybridization, which accounted for

the short distances observed. Fig. 9b shows an ABF-STEM image of a twinned nanoparticle. The twinned nanoparticle is imaged along the [011] zone axis, and twinning occurs over a {111}-type twin plane, which is characteristic of cubic structures.

From the observation of a well-ordered cubic framework of Mn in Li4 and Li0 *via* combined Rietveld refinement, x-PDF and TEM, and the identical coherent domain sizes of ~6 nm in both compounds, we conclude that there are no major structural rearrangements of the Li4 material during lithium extraction. Thus, it seems unlikely that the Mn^{4+}/Mn^{5+} redox couple can be responsible for the electrochemical activity at 4 V (Fig. 4). This scenario would entail major structural rearrangements for the accommodation of Mn^{5+} in a tetrahedral environment, which were not observed.

The formation of oxo-peroxo groups from possible dimerization at high potentials in the oxidized material[33,34] and the formation of electron holes on the oxygen ligands have not been directly observed in this study and are particularly difficult to detect in intrinsically disordered compounds. However, we strongly believe that the participation of oxygen in the electrochemical activity of the Li4–Li_2O composite *via* the strong hybridization of the TM–oxygen bond that can in turn explain the displacement of certain oxygen atoms towards the Mn column, as observed by TEM, may be responsible for the additional capacity observed at 4 V.

Conclusions

In this study, we have identified the presence of Li_2O in the Li4–Li_2O composite and the composition of the main Li4 rock salt material *via* a thorough compositional analysis combining ICP with combined neutron and synchrotron X-ray Rietveld refinement. It was demonstrated that the presence of 7 wt% Li_2O in the initial positive intercalation electrode was responsible for the exceptional reversible capacity of 275 mA h g^{-1} during cycling, with an increase in capacity of 30% with respect to that of the Li4 material. Interestingly, Li_2O was found to react with Li4 during the course of the first charge cycle with substantial irreversibility. Structural characterization of the pristine and oxidized phases was carried out *via* a combined x-PDF, HAADF-STEM, and ABF-STEM study. A reduction in the volume of the cell upon delithiation was observed from Li4 to Li0, whereas the average structure remained that of a rock-salt MnO structure. The absence of major structural rearrangements upon the delithiation of Li4 and the short Mn–O distances in Li0 observed by TEM suggest strong hybridization of the TM–oxygen, suggesting a redox mechanism involving a combination of manganese and oxygen redox activity.

Conflicts of interest

There are no conflicts of interest to declare.

Author contributions

M. F. and V. P. contributed to the synthesis of the materials and performed the electrochemical and chemical analyses. M. F., A. M. and C. V. C. performed the magnetic analysis of the samples. M. D. L., P. B. and D. C. analyzed the neutron, PDF, and XRPD data, and O. I. L. and A. L. C. carried out the TEM analysis. C. J., P. B., and V. P. conceived and designed the project. All the authors contributed to writing the paper.

Acknowledgements

The authors gratefully acknowledge S. Eichendorff, F. Veillon and S. Gascoin for technical help and N. Boudet, N. Blanc and V. Nassif for assistance in the synchrotron and neutron experiments. This work was supported by the ANR grant ANR15-CE05-0006-01 DAME.

Notes and references

1 B. L. Ellis, K. T. Lee and L. F. Nazar, *Chem. Mater.*, 2010, **22**, 691–714.
2 N. Nitta, F. Wu, J. T. Lee and G. Yushin, *Mater. Today*, 2015, **18**, 5.
3 J. B. Goodenough and Y. Kim, *Chem. Mater.*, 2010, **22**, 587–603.
4 J. M. Tarascon, *Philos. Trans. R. Soc., A*, 2010, **368**, 3227–3241.
5 B. Melot and J. M. Tarascon, *Acc. Chem. Res.*, 2013, **46**, 1226–1238.
6 V. Pralong, *Prog. Solid State Chem.*, 2009, **37**, 262–277.
7 R. J. Gummow, A. De kock and M. M. Thackeray, *Solid State Ionics*, 1994, **69**, 59–67.
8 S. Patoux, L. Daniel, C. Bourbon, H. Lignier, C. Pagano, F. Le Cras, S. Jouanneau and S. Martinet, *J. Power Sources*, 2009, **189**, 344–352.
9 F. Capitaine, P. Gravereau and C. Delmas, *Solid State Ionics*, 1996, **89**, 197–202.
10 J. M. Paulsen, C. L. Thomas and J. R. Dahn, *J. Electrochem. Soc.*, 1999, **146**, 3560–3565.
11 Y. He, Q. Feng, S. Zhang, Q. Zou, X. Wu and X. Yang, *ACS Sustainable Chem. Eng.*, 2013, **1**, 570–573.
12 K. Kubota, T. Kaneko, M. Hirayama, M. Yonemura, Y. Imanari, K. Nakane and R. Kanno, *J. Power Sources*, 2012, **216**, 249–255.
13 S. F. Amalraj, B. Markovsky, D. Sharon, M. Talianker, E. Zinigrad, R. Persky, O. Haik, J. Grinblat, J. Lampert, M. Schulz-Dobrick, A. Garsuch, L. Burlaka and D. Aurbach, *Electrochim. Acta*, 2012, **78**, 32–39.
14 A. R. Armstrong, A. D. Robertson and P. G. Bruce, *J. Power Sources*, 2005, **146**, 275–280.
15 T. Ohzuku and Y. Makimura, *Chem. Lett.*, 2001, **7**, 642–643.
16 H. Koga, L. Croguennec, M. Ménétrier, P. Mannessiez, F. Weill and C. Delmas, *J. Power Sources*, 2013, **236**, 250–258.
17 H. Koga, L. Croguennec, M. Ménétrier, K. Douhil, S. Belin, L. Bourgeois, E. Suard, F. Weill and C. Delmas, *J. Electrochem. Soc.*, 2013, **160**, A786–A792.
18 F. Weill, N. Tran, L. Croguennec and C. Delmas, *J. Power Sources*, 2007, **172**, 893–900.
19 J. S. Kim, C. S. Johnson and M. M. Thackeray, *Electrochem. Commun.*, 2002, **4**, 205–209.

20 N. Yabuuchi, K. Yoshii, S. T. Myung, I. Nakai and S. Komaba, *J. Am. Chem. Soc.*, 2011, **133**, 4404–4419.
21 T. Ohzuku, M. Nagayama, K. Tsuji and K. Ariyoshia, *J. Mater. Chem.*, 2011, **21**, 10179–10188.
22 A. D. Robertson and P. G. Bruce, *Electrochem. Solid-State Lett.*, 2004, **7**, A294–A298.
23 A. R. Armstrong, M. Holzapfel, P. Novak, C. S. Johnson, S. H. Kang, M. M. Thackeray and P. G. Bruce, *J. Am. Chem. Soc.*, 2006, **128**, 8694–8698.
24 N. Yabuuchi, M. Takeuchi and M. Nakayama, *PNAS*, 2015, **112**, 7650–7655.
25 J. M. Tarascon, G. Vaughan, Y. Chabre, L. Seguin, M. Anne, P. Strobel and G. Amatucci, *J. Solid State Chem.*, 1999, **147**, 410–420.
26 Z. Lu and J. R. Dahn, *J. Electrochem. Soc.*, 2002, **149**, A815–A822.
27 Y. Okamoto, *J. Electrochem. Soc.*, 2012, **159**, A152–A157.
28 K. Luo, M. R. Roberts, R. Hao, N. Guerrini, M. D. Pickup, Y. S. Liu, K. Edström, J. Guo, A. V. Chadwick, L. C. Duda and P. G. Bruce, *Nat. Chem.*, 2016, **8**, 684–691.
29 A. Urban, J. Lee and G. Ceder, *Adv. Energy Mater.*, 2014, **4**, 1400478(too large a number?).
30 M. Sathiya, G. Rousse, K. Ramesha, C. P. Laisa, H. Vezin, M. Sougrati, M. L. Doublet, D. Foix, D. Gonbeau, W. Walker, A. S. Prakash, M. Ben Hassine, L. Dupont and J. M. Tarascon, *Nat. Mater.*, 2013, **12**, 827–835.
31 M. Sathiya, A. M. Abakumov, D. Foix, G. Rousse, K. Ramesha, M. Saubanère, M. L. Doublet, H. Vezin, C. P. Laisa, A. S. Prakash, D. Gonbeau, G. Van Tendeloo, R. Dominko and J. M. Tarascon, *Nat. Mater.*, 2015, **14**, 230–238.
32 E. McCalla, A. M. Abakumov, M. Saubanère, D. Foix, E. J. Berg, G. Rousse, M. L. Doublet, D. Gonbeau, P. Novák, G. Van Tende-loo, R. Dominko and J. M. Tarascon, *Science*, 2015, **350**, 1516–1521.
33 M. Saubanère, E. McCalla, J. M. Tarascon and M. L. Doublet, *Energy Environ. Sci.*, 2016, **9**, 984–991.
34 H. Chen and M. S. Islam, *Chem. Mater.*, 2016, **28**, 6656–6663.
35 M. S. Whittingham, *Dalton Trans.*, 2008, **0**, 5424–5431.
36 S. T. Myung, K. Amine and Y. K. Sun, *J. Power Sources*, 2015, **238**, 219–236.
37 M. Freire, N. V. Kosova, C. Jordy, O. I. Lebedev, D. Chateigner, A. Maignan and V. Pralong, *Nat. Mater.*, 2016, **15**, 173–177.
38 P. Pangaud, S. Basolo, N. Boudet, J. F. Berar, B. Chantepie, J. C. Clemens, P. Delpierre, B. Dinkespiler, K. Medjoubi, S. Hustache, M. Menouni and C. Morel, *Nucl. Instrum. Methods Phys. Res., Sect. A*, 2008, **591**, 159–162.
39 G. Ashiotis, A. Deschildre, Z. Nawaz, J. P. Wright, D. Karkoulis, F. E. Picca and G. Kieffer, *J. Appl. Crystallogr.*, 2014, **40**, 510–519.
40 J. Rodríguez-Carvajal, *Phys. B*, 1993, **192**, 55–69.
41 P. Juhas, T. Davis, C. L. Farrow and S. J. L. Billinge, *J. Appl. Crystallogr.*, 2013, **46**, 560–566.
42 C. L. Farrow, P. Juhas, J. W. Liu and S. J. L. Billinge, *J. Phys.: Condens. Matter*, 2007, **19**, 1–7.
43 S. Malifarge, B. Delobel and C. Delacourt, *J. Electrochem. Soc.*, 2017, **164**(14), A3925–A3932.
44 E. Talaie, P. Bonnick, X. Sun, Q. Pang, X. Liang and L. F. Nazar, *Chem. Mater.*, 2017, **29**, 90–105.
45 J. Xie, N. Imanishi, T. Zhang, A. Hirano, Y. Takeda and O. Yamamoto, *Electrochim. Acta*, 2009, **54**, 4631–4637.
46 P. Thompson, D. E. Cox and J. B. Hastings, *J. Appl. Crystallogr.*, 1987, **20**, 79–83.
47 R. D. Shannon, *Acta Crystallogr.*, 1976, **A32**, 751–767.